

A multi-element interstitial ultrasound applicator for the thermal therapy of brain tumors

Michael S. Canney^{a)}

CarThera, Brain and Spine Institute, Pitié Salpêtrière Hospital, 47-83 Boulevard de l'Hôpital, 75013 Paris, France

Françoise Chavier

Inserm, U1032, LabTau, University Lyon 1, 151 Cours Albert Thomas, 69424 Lyon Cedex 03, France

Sergey Tsysar

Department of Acoustics, Faculty of Physics, Moscow State University, Moscow 119992, Russia

Jean-Yves Chapelon and Cyril Lafon

Inserm, U1032, LabTau, University Lyon 1, 151 Cours Albert Thomas, 69424 Lyon Cedex 03, France

Alexandre Carpentier

Paris 6 University, 47-83 Boulevard de l'Hopital, 75013 Paris, France

(Received 28 September 2012; revised 3 April 2013; accepted 11 April 2013)

Interstitial thermal therapy is a minimally invasive treatment modality that has been used clinically for ablating both primary and secondary brain tumors. Here a multi-element interstitial ultrasound applicator is described that allows for increased spatial control during thermal ablation of tumors as compared to existing clinical devices. The device consists of an array of 56 ultrasound elements operating at 6 MHz, oriented on the seven faces of a 3.2 mm flexible catheter. The device was first characterized using the acoustic holography method to examine the functioning of the array. Then experiments were performed to measure heating in tissue-mimicking gel phantoms and *ex vivo* tissue samples using magnetic resonance imaging-based thermometry. Experimental measurements were compared with results obtained using numerical simulations. Last, simulations were performed to study the feasibility of using the device for thermal ablation in the brain. Experimental results show that the device can be used to induce a temperature rise of greater than 20 °C in *ex vivo* tissue samples and numerical simulations further demonstrate that tumors with diameters of greater than 30-mm could potentially be treated. © 2013 Acoustical Society of America. [<http://dx.doi.org/10.1121/1.4812883>]

PACS number(s): 43.80.Sh [CCC]

Pages: 1647–1655

I. INTRODUCTION

Thermal therapy is a treatment option for patients with brain tumors that has been investigated in recent clinical trials for those who fail or who are ineligible for conventional treatments (i.e., surgical resection, radiotherapy, and chemotherapy). Interstitial devices that use radiofrequency¹ or lasers^{2–6} and extracorporeal ultrasound devices⁷ have been developed and used to locally raise the temperature in brain tumors to greater than 60 °C to induce either partial or complete necrosis of the malignant tissue volume.

Among the various techniques for performing thermal ablation in the brain, laser interstitial thermal therapy (LITT) has been the mostly widely used in recent clinical studies.^{2,3,6} LITT is performed by first drilling a 5–10 mm burr hole in the skull followed by stereotactic implantation of a 2–3 mm diameter laser applicator into the center of the tumor to be treated.⁸ After insertion of the laser fiber, the patient is placed within a magnetic resonance imaging (MRI) scanner, where real-time temperature mapping is

performed during laser heating and used to predict cell death.⁹ Tumors with sizes of 9–25 mm in diameter have been treated with this technique by heating with laser applicators for durations of 2–10 min.²

Although LITT has been shown to be a promising treatment option for many patients, current devices have a limited ability to fully treat many tumor geometries. LITT applicators typically use a laser source with a diffusing fiber tip that has a spherical or ellipsoidal distribution of heating.² For tumor geometries that do not conform well with this heating pattern, the surgeon must either manually translate the laser fiber, perform multiple insertions of the device into the tumor,⁴ or be limited to performing partial treatments of the affected region.⁶

To overcome these limitations, there are several different technologies in development to perform thermal ablation in the brain with increased spatial control. For example, a focused laser system has been developed with a small region of heating that can be mechanically steered over the treatment volume to achieve conformal ablation.^{4,5} Although this device allows for increased spatial control, the reported treatment times are long (on the order of several hours) as the device must be scanned slowly over the entire tumor volume.⁴

^{a)}Author to whom correspondence should be addressed. Electronic mail: michael.canney@carthera.eu

Another approach that is in development is the use of transcranial focused ultrasound.^{7,10,11} This approach uses large hemispherical ultrasound arrays consisting of hundreds to thousands of individual ultrasound elements and allows for heating in the brain without requiring surgical opening of the skull. Although promising, there have not yet been any reports of successful brain tumor treatments in patients.¹¹

In this work, our goal was to develop a heating device that uses an interstitial approach with an ultrasound-based applicator. Various designs of miniature therapeutic ultrasound transducers have been proposed for performing thermal ablation via endovascular,¹² interstitial,^{13,14} and transesophageal¹⁵ access for treatments in the heart,¹⁴ liver,^{16,17} brain,^{12,18} and other organs. These devices have diameters ranging from 3 to 10 mm and operate at frequencies of 3–10 MHz. Interstitial therapeutic ultrasound applicators in particular have been built and tested using a variety of designs by several different groups and include single-element^{19,20} and multi-element designs with planar^{21–24} and cylindrical^{18,25} elements.

While multi-element interstitial ultrasound applicators have been demonstrated previously, they have typically used an MR-compatible rotational system for performing ablation of a full three-dimensional tissue volume²³ or lack the ability to control heating along the axis of the probe.^{18,26} In this work, an applicator was designed to avoid mechanical translation and rotation while allowing for the possibility to control heating both along the applicator axis and in the plane perpendicular to the applicator. To achieve this goal, a device with 56 planar ultrasound elements oriented on a multifaceted catheter was constructed and tested. Experimental measurements and numerical simulations were further used to investigate the feasibility of using this new device design to perform thermal ablation in the brain.

II. MATERIALS AND METHODS

The multi-element interstitial ultrasound device was first characterized acoustically. The acoustic holography method was used to reconstruct the source vibration to characterize the acoustic output of the device. Next, numerical simulations were performed of the acoustic and thermal field and compared with experimental results of heating in gel phantoms and *ex vivo* brain tissue samples using MR thermometry. Finally, the numerical model was used to simulate the expected characteristics of *in vivo* heating with the device.

A. Ultrasound device

The prototype ultrasound device, shown in Fig. 1(a), consisted of an array of 56 piezocomposite ultrasound elements, each 1 mm × 1 mm, oriented on a 3.2-mm semi-flexible support, and operated at 6 MHz (Imasonic, Voray sur l'Ognon, France). The elements were arranged with eight elements on each face of a heptagon with a gap of 0.25 mm between each element. The center of the transducer had a 1 mm diameter center channel that was used for circulating degassed, room temperature (20 °C) water for actively cooling the piezocomposite ultrasound elements. Water entered the central channel of the transducer support, exited at the



FIG. 1. (Color online) (a) A photograph of one of the the multi-element MR-compatible interstitial ultrasound transducers used in experiments. The transducer had 56 planar piezocomposite ultrasound elements, each 1 mm × 1 mm, oriented on a heptagon with eight elements on each face and was operated at 6 MHz. The 3.2-mm diameter ultrasound transducer fit within an external cooling sheath (b) that had an outer diameter of 4.8 mm.

tip, and recirculated back over the front faces of the elements through the external cooling sheath that is shown in Fig. 1(b). The cooling sheath had an outer diameter of 4.8 mm and was constructed from a 130- μ m thick polyimide tube (Dixi Microtechniques, Besançon, France). The flow for the cooling circuit was driven by a peristaltic pump (MasterFlex, Cole Parmer Instruments, Chicago, IL) at a flow rate of 40 ml/min.

Two different prototypes were constructed that consisted in essentially the design described in the preceding text but with a partially functioning version with fewer elements followed by a fully functioning version. The first prototype had only three active faces (24 elements), and a subsequent prototype had all seven faces (56 elements) active. The element size, spacing, frequency, and mechanical design were identical in both versions. The three-face prototype was used in preliminary testing of the array, and the acoustic holography measurements described in the following text were performed using this prototype to verify the functioning of the array. The seven-face prototype was used in subsequent *in vitro* MR heating experiments described in the following text. To operate the seven-face prototype, a 16-channel radiofrequency generator (Image Guided Therapy, Bordeaux, France) was used. The transducer was connected using 14 of the channels so that four elements on each face were wired in parallel. For each of the 14 channels, a matching circuit was constructed to match the electrical impedance to 50 Ω . This configuration allowed for complete computer control of each face of the transducer using two channels of the generator without physically changing wiring configurations.

Radiation force balance measurements were performed to measure the acoustic power output of the transducer. Measurements were performed by driving all of the elements of a single face at the same time using two channels of the generator. An absorbing target (Aptflex F21, Precision Acoustics, Dorchester, UK), suspended above the transducer, was used with a microgram balance (Model CP64, Sartorius, Germany) for the measurements, which were performed with the cooling sheath attached to the transducer in a water bath at room temperature (20 °C). The acoustic intensity levels quoted herein are the average output intensity levels at the surface of the array and were calculated by dividing the measured acoustic power output measured by the force

balance by the assumed active area of each face (eight elements), which was 8 mm².

B. Acoustic holography measurements

To study the acoustic output of the prototype device, the acoustic holography method²⁷ was used to reconstruct the source vibration for one of the prototypes. For these measurements, a hydrophone (Onda HGL-0200 with AH-2010 preamplifier, Onda Corporation, Sunnyvale, CA) was used to scan a two-dimensional (2D) plane parallel to the transducer face at a distance of 6 mm. The measurement plane was chosen to be from $x = -2.5$ – 2.5 mm and $y = -9$ – 9 mm with a step size of 0.1 mm. Each face of the transducer was driven using a function generator (16 V_{pp}, 60 cycle burst, 5 kHz PRF, HP 8116A, Hewlett Packard, Palo Alto, CA) with all eight elements in parallel, and the pressure waveforms were averaged using a digital oscilloscope (Model WS422, Lecroy, Chestnut Ridge, NY). The measured amplitude and phase in the measurement plane were used to reconstruct the amplitude and phase distribution on each face of the transducer surface, S , using the Fourier method.²⁸ With this method, the spatial spectrum pressure $P(k_x, k_y, z)$ on the transducer surface S can be found by multiplying the measured pressure field $P(k_x, k_y, z_m)$ by a propagator function $G(k_x, k_y, z - z_m)$

$$G(k_x, k_y, z - z_m) = e^{i\sqrt{k^2 - k_x^2 - k_y^2}(z - z_m)}, \quad (1)$$

where $k = w/c$ is the wave number, and k_x and k_y are the components of the wave vector in the x and y directions. The spatial spectra and corresponding pressure fields are then related to each other via the two-dimensional Fourier transform

$$P(k_x, k_y, z) = \int_{-\infty}^{\infty} \int_{-\infty}^{\infty} p(x, y, z) e^{-i(k_x x + k_y y)} dx dy, \quad (2)$$

$$p(x, y, z) = \frac{1}{(2\pi)^2} \int_{-\infty}^{\infty} \int_{-\infty}^{\infty} P(k_x, k_y, z) e^{i(k_x x + k_y y)} dk_x dk_y. \quad (3)$$

Because the inverse problem is ill-posed due to possible exponential growth of errors, the region of interest was restricted by only the radiation circle so that the values k_x and k_y satisfy the expression: $k_x^2 + k_y^2 < k^2$. Calculations were performed using 2D fast Fourier transform with additional zero padding of measurement results.

In the case of high frequency holography measurements as performed herein, two difficulties arise. First, due to a large scanning grid and a relatively long scanning procedure (here, the scan time was approximately 3 h), it is necessary to avoid changes in the speed of sound due to temperature changes of the water. This problem can be solved by using a large water tank or using temperature control tools. Second, at higher frequencies, errors of relative positioning of the measurement plane and the transducer surface are increased relative to a wavelength. In the case of significant errors, special methods can be applied in the reconstruction

process.²⁹ If the angular deviation is less than $\approx 2^\circ$, a simple algorithm can be used to achieve an optimal reconstruction: A small phase correction can be applied to the measured results by adding a small value of $ky \tan(\theta_1)$ along the y axis and $kx \tan(\theta_2)$ along the x axis before the reconstruction where θ_1 and θ_2 are the angle of inclination between the measurement plane at $z_m = 6$ mm and the reconstruction plane at $z = 0$ mm. This method was used to achieve an optimal reconstruction of the transducer in the results shown.

C. MRI heating experiments

Measurements of the temperature rise during heating using the seven-face prototype were performed in a 1.5 T clinical MRI (Signa Excite, General Electric Medical Systems, Milwaukee, WI). An experimental apparatus was built to hold the sample and ultrasound probe in a standard birdcage style head imaging coil. An echoplanar gradient echo sequence (echo time = 40 ms, repetition time = 575 ms, field of view = 240×240 mm, acquisition matrix = 128×128 , slice thickness = 3 mm, voxel size = $1.875 \text{ mm} \times 1.875 \text{ mm} \times 3 \text{ mm}$) was used to acquire seven imaging planes, each oriented perpendicular to the probe and centered in the middle of the active array, for three-dimensional coverage of the heated volume. An acquisition of complex image pairs in this 3D volume was obtained every 5.5 s during heating. The acquired images were processed using custom software written in MATLAB (Mathworks, Natick, MA). The proton resonance frequency (PRF) method³⁰ was used to calculate temperature changes in the sample during heating using a PRF coefficient of $-0.01 \text{ ppm}/^\circ\text{C}$. Complex phase subtraction³¹ was performed for each image pair in time, and phase drift was corrected for by subtracting the phase from an unheated region in each sample. Temperature images were additionally masked using a threshold criterion based on the magnitude of the first acquired image set in the EPI sequence and were overlaid on either magnitude images taken from the same EPI sequence or on high resolution T1-w anatomical images acquired in the same imaging planes. The ultrasound generator was placed outside of the faraday cage in the MR control room, and 14 9-m coaxial cables connected the generator to the matching network, which was placed on the floor next to the treatment bed. Each of the coaxial cables was grounded to the faraday cage at entry into the MR room. The pump for circulating cooling water for the transducer was placed in the console room, and 2 10-m tubes connected the cooling circuit to the probe. Heating experiments were performed using a 100 ml, 5-cm diameter, 18% BSA gel phantom³² and fresh, degassed bovine brain samples. The samples were placed in a water bath at room temperature for experiments.

D. Numerical modeling

Both acoustic and thermal modeling of the device was performed to observe the variations in heating and lesion size with changes in operating parameters. Acoustic modeling was first performed by numerical solution of the Rayleigh integral with a spatial discretization for the surface of the transducer of 50 μm and a pressure attenuation coefficient, α , as shown in Table I. Thermal modeling was

TABLE I. Parameters used in numerical simulations.^{32–34} *A range of parameters for the attenuation and mass flow rate were used in the additional simulations shown in Fig. 8.

| | | | Tissue phantom | Brain (cow) | Brain (human) |
|----------------------|------------|------------------------|----------------|-------------|---------------|
| Sound speed | c | m/s | 1500 | 1500 | 1500 |
| Density | ρ | kg/m ³ | 1044 | 1040 | 1040 |
| Thermal conductivity | k | W/(m·°C) | 0.72 | 0.5 | 0.5 |
| Specific heat | C | J/(kg·°C) | 5300 | 3640 | 3640 |
| Attenuation | α | dB/cm @ 6 MHz | 2.0 | 2.8 | 3.7 (2–6)* |
| Mass flow rate | w | kg/(m ³ ·s) | 0 | 0 | 10 (0–20)* |
| Sample temperature | T_∞ | °C | 20 | 20 | 37 |

performed by numerical solution of the Bioheat Equation using a finite difference scheme

$$\rho C \frac{\partial T}{\partial t} = k \nabla^2 T - wC(T - T_\infty) + Q, \quad (4)$$

where T is the temperature of the tissue, T_∞ is the ambient temperature of the tissue, C is the specific heat of the tissue, k is the thermal conductivity, Q is the heating due to absorption of ultrasound in tissue ($Q = \beta \alpha p^2 / \rho c$), and w is the mass flow rate of blood in tissue and β is the ratio of absorption to attenuation, which was assumed to be equal to one in all simulations performed herein. The parameters used in simulations are specified in Table I. Numerical simulation of Eq. (4) was performed using a Crank–Nicolson method with a spatial grid of 0.25 mm and a temporal step of 33 ms. The simulated temperature measurements were additionally spatially averaged over the discretization grid to a size of $1.75 \times 1.75 \times 3$ mm for better comparison with the MR-derived temperature, where the voxel size was significantly larger ($1.875 \times 1.875 \times 3$ mm) than the $0.25 \times 0.25 \times 0.25$ mm spacing used in simulations.

Simulations were first performed incorporating the results from acoustic holography measurements to compare the heating induced by an “ideal” transducer with the actual measured boundary condition. Following these simulations, additional simulations were performed in tissue phantoms and *ex vivo* tissue to compare with experimental results from heating experiments in the MR. Finally, *in vivo* simulations were performed to estimate the size of lesions that can be produced with the applicator. For *in vivo* simulations, the thermal dose was used to estimate the extent of the lesion size

$$t_{43} = \sum_{t=0}^{t=final} R^{(43-T)} \Delta t, \quad (5)$$

where t_{43} is the thermal dose in equivalent minutes at 43 °C, T is the average temperature during the time step Δt , and R is a constant equal to 0.5 at temperatures above 43 °C and equal to 0.25 below 43 °C. Lesion sizes were estimated and compared using a threshold of $t_{43} = 50$ or 240 min. While $t_{43} = 240$ min is conventionally used in HIFU therapies in many organs, a lower threshold has been reported in the brain by several groups with values of $t_{43} = 17$ –60 min.^{18,35–38} Values of 50 and 240 min were used to compare the difference in lesion size when using two different threshold values.

III. RESULTS

A. Acoustic holography measurements

An example of the measured amplitude and phase for one face of one applicator and the results after reconstruction of the source vibration using the acoustic holography method are shown in Fig. 2. A small angular correction was applied to the measured phase as described in Sec. II, using values of $\theta_1 = 0^\circ$ and $\theta_2 = 0.85^\circ$ for the face shown. This measurement and reconstruction process was repeated for each of the 3 faces of one of the three-face prototype transducers to study the output of the device and was subsequently used to simulate the pressure along the axis perpendicular to the transducer as shown in Fig. 3. It can be observed that there is slightly more energy output from the elements in the center of the actual transducer than for the “ideal” case where the energy is distributed evenly over all of the elements. This same effect was observed for all of the faces of the transducer measured and appeared to be inherent in the construction of the applicator.

The calculated pressure distributions from reconstruction of the surface vibration were subsequently used as an input to Eq. (4) to simulate the effect of this uneven power output on the heating distribution using the parameters for an 18% BSA gel phantom, Table I. An acoustic power of

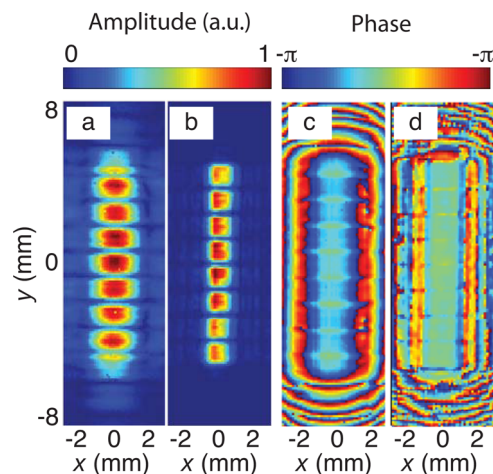


FIG. 2. (Color online) The measured amplitude (a) and phase (c) at a plane 6 mm in front of one face of the transducer. The measurements were used to reconstruct the amplitude (b) and phase (d) at the transducer surface using Eqs. (1) to (3). All eight elements of one of the transducer face can be observed in the reconstructed amplitude shown in (b).

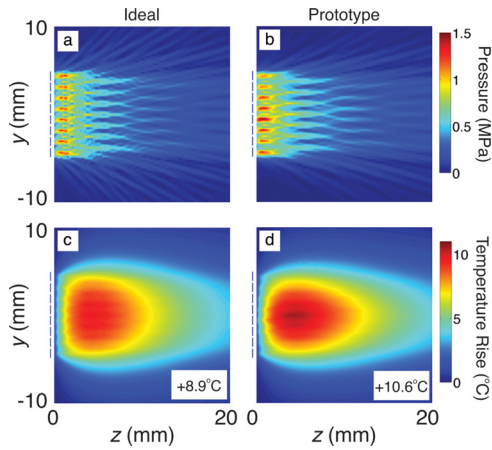


FIG. 3. (Color online) A comparison of the pressure fields calculated using an “ideal” transducer with a uniform pressure distribution over the eight elements of a face (a) and using the actual reconstructed surface vibration (b) shown in Figs. 2(b) and 2(d). The two pressure distributions were further used as an input for modeling the heating in a simulated tissue phantom using Eq. (4). An equivalent acoustic power of 1.6 W (20 W/cm^2 average surface intensity) was used and a heating duration of 120 s was simulated. At the end of the heating, the maximum temperature rise with the prototype transducer was slightly higher ($+10.6^\circ\text{C}$) than with the “ideal” transducer ($+8.9^\circ\text{C}$).

1.6 W (20 W/cm^2 equivalent surface intensity) was used, and the resulting temperature distributions showed a slightly higher temperature for the transducers with uneven energy distribution and led to a maximum temperature rise of 8.9°C (ideal) and 10.6°C for the simulations of the transducers using a “nonideal” vibration as the source boundary condition. Simulations for the other two faces (not shown) resulted in a similar enhancement of heating due to increased output by the center elements and also showed that the maximum temperature for a single face shifted slightly from the center during heating along the transducer axis. Despite these small differences, the simulations using the seven-face applicator (used in MR heating tests in the following text) were performed assuming the ideal transducer vibration because all faces of the seven-face transducer were not measured using the acoustic holography method.

B. MR heating tests

The MR compatibility of the device was studied using spin echo as well as using the EPI thermal sequence. On spin echo sequences, there was no artifact observed. On the EPI sequence, there was a small artifact that extended approximately 1 pixel (1.875 mm) from the transducer in the active region and up to several pixels on the sides next to the active section for a maximum artifact of 10 mm. A magnitude image from the EPI sequence is shown in Fig. 4 in the planes along the transducer (a) and perpendicular to it (b). The small artifact in the active region permitted imaging of the temperature within ≈ 2 mm of the transducer face.

Heating was performed in tissue-mimicking phantoms using MR thermometry to monitor the temperature rise and was compared with numerical simulations. Three different heating configurations were tested and are shown in Fig. 5: One face firing for 120 s, two adjacent faces firing for 120 s,

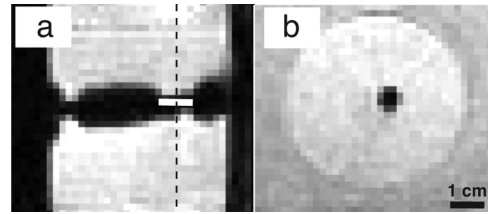


FIG. 4. MR compatibility of the transducer determined using the echoplanar gradient echo sequence that was used for thermometry. The magnitude image from the sequence with the slice oriented along the transducer (a) and perpendicular to the transducer (b) are shown. The image in (b) was taken at the slice positioned at the dashed line in (a). The MR artifact with this sequence extended ≈ 1 pixel (1.875 mm) from the probe near the active section of the catheter, which is shown by the white line in (a). Each pixel in the images shown had a size of $1.875 \text{ mm} \times 1.875 \text{ mm}$ in the imaging plane with a slice thickness of 3 mm.

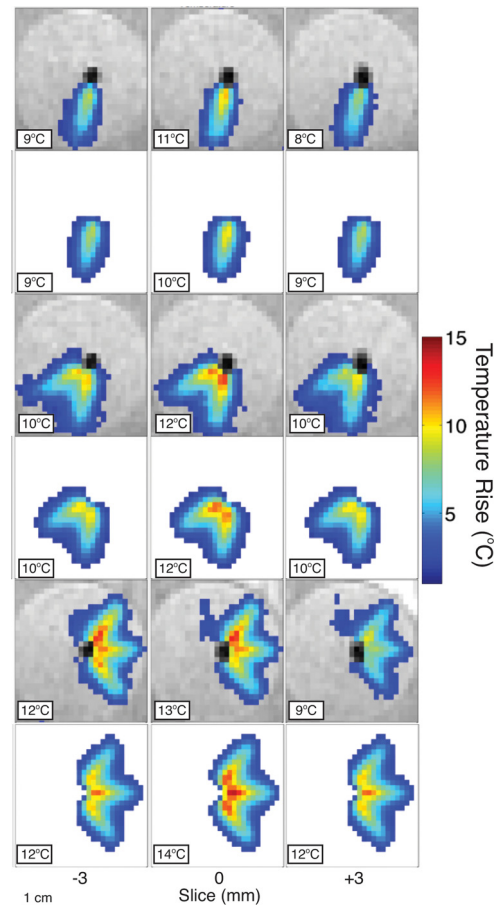


FIG. 5. (Color online) *In vitro* heating patterns of the device measured using MR thermometry and simulated using the numerical model. Measurements were performed in a 1.5 T MRI using a seven-slice gradient echo echoplanar sequence with a slice spacing of 3 mm and a voxel size of $1.875 \text{ mm} \times 1.875 \text{ mm} \times 3 \text{ mm}$. The probe was inserted into a 5-cm diameter, 18% BSA gel phantom for experiments. The calculated temperature maps for three slices centered at the active section of the probe are overlaid on the magnitude image acquired during the same sequence. Three different heating profiles are shown using: One face (20 W/cm^2 , 120 s), two faces (20 W/cm^2 , 120 s), or three faces (20 W/cm^2 , 120 s) of the transducer. Note that the various faces were activated electronically and no rotation of the probe was performed between experiments. The maximum temperature rise obtained in each slice for the model and measurement are shown in the corner of each image.

and three faces firing for 120 s. In all three cases, the surface intensity was 20 W/cm^2 . The maximum temperature rise in each case was $+12^\circ\text{C}$ (one active face), $+12^\circ\text{C}$ (two active faces), and $+13^\circ\text{C}$ (three active faces) for the experimental data. The experimental data were compared with numerical modeling of the same conditions and are also shown below each experimental measurement for three different imaging planes oriented perpendicular to the axis of the applicator and centered at the middle of the array. The maximum temperature rise for the simulated result (averaged over the size of the MR voxel) was $+10^\circ\text{C}$ (one active face), $+12^\circ\text{C}$ (two active faces), and $+14^\circ\text{C}$ (three active faces) and was in good agreement with experimental measurements. The general form of the heated zone measured on MRI was also in good agreement with the numerical model indicating that heating by the transducer could be well-predicted using the numerical model.

Heating was also performed in degassed *ex vivo* bovine brain samples at a higher output intensity of 30 W/cm^2 for 240 s. The results are shown in Fig. 6. The maximum temperature rise in experiments was $+29^\circ\text{C}$. The experiments were performed to demonstrate the possibility to reach therapeutic temperature levels with the applicator and to monitor temperature changes with the MRI. The higher temperatures induced agree well with the fact that the absorption in brain is expected to be approximately $1.5\times$ higher in bovine brain than in the tissue-mimicking gel phantoms and that the output intensity here was also 50% greater. Simulations were also performed using the parameters in Table I and resulted in a similar magnitude of temperature rise of $+32^\circ\text{C}$, although it can be observed that there is more discrepancy between the simulation and the measurement due to the inhomogeneity of the brain tissue sample.

C. Numerical simulations of heating using brain tissue parameters

Numerical simulations of heating were performed using the acoustic and thermal properties of human brain shown in Table I. The results of simulations are shown in Fig. 7, which shows the estimated thermal lesion after heating using an output of 30 W/cm^2 for 240 s with all elements of the

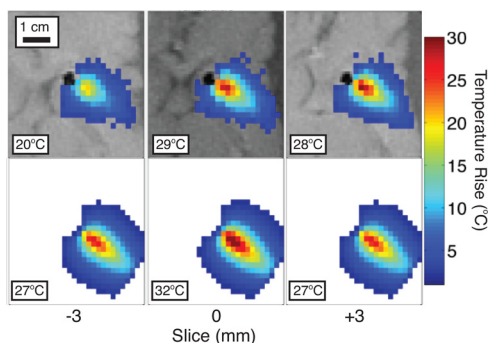


FIG. 6. (Color online) Measurements (top) and simulations (bottom) of heating in an *ex vivo* bovine brain tissue sample. The calculated temperature maps for three slices are overlaid on a high resolution T1w spin echo image acquired before heating. Heating was performed using a single face operating at 30 W/cm^2 for 240 s. The maximum temperature in each slice is shown in the corner of each figure.

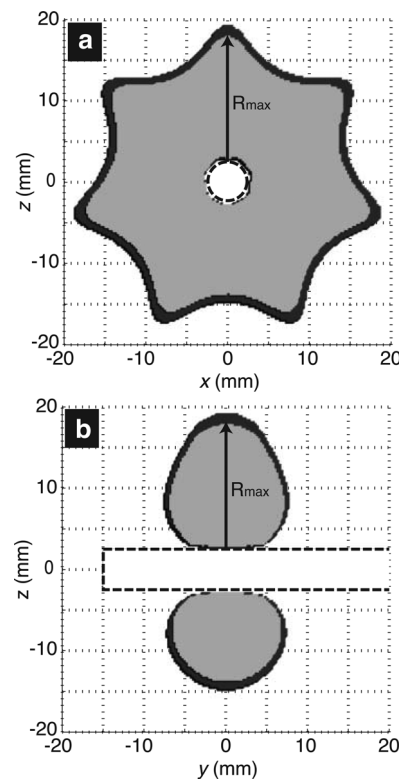


FIG. 7. The simulated thermal lesion produced after heating using all seven faces *in vivo* for 240 s at 30 W/cm^2 . (a) A depiction of the shape of the thermal lesion oriented perpendicular to the axis of the applicator at $y = 0$. (b) A depiction of the shape of the thermal lesion oriented along the applicator, at $x = 0$. The two colors indicate different thermal dose thresholds for comparison. The gray indicates a dose of $t_{43} = 240 \text{ min}$ while the black indicates the dose contour with a lower threshold of $t_{43} = 50 \text{ min}$.

device operating simultaneously. A depth of $>15 \text{ mm}$ is reached during this heating duration and the estimated maximum temperature reached is 95°C . Additional simulations were performed at a lower intensity of 20 W/cm^2 and demonstrated that a 15 mm treatment depth can also be reached at a lower output level, but a longer heating duration is required of more than 9 min. The simulated lesions are plotted with two different thermal dose thresholds of $t_{43} = 50$ and 240 min. The results show that the difference between the two lesion thresholds results in only $\approx 1\text{-mm}$ difference using these two different dose thresholds, indicating that there is relative insensitivity to the dose used in the evaluation of the final lesion size under these operating conditions.

Additional numerical simulations of heating using a range of brain tissue parameters are presented in Fig. 8. In these simulations, it was assumed that the applicator was operating with all 56 elements active at a frequency of 6 MHz and at an output surface intensity of 30 W/cm^2 , similar to the results shown in Fig. 7. In contrast to using a fixed attenuation, perfusion, and heating duration as shown in the results plotted in Fig. 7, the result of varying these parameters was investigated.

In Fig. 8(a), the effect of variations in the tissue attenuation and heating duration was first considered. The mass flow rate, accounting for perfusion in the tissues, was maintained constant at $w = 10 \text{ kg/(m}^3\cdot\text{s)}$ and simulations of heating were performed using a range of tissue attenuation

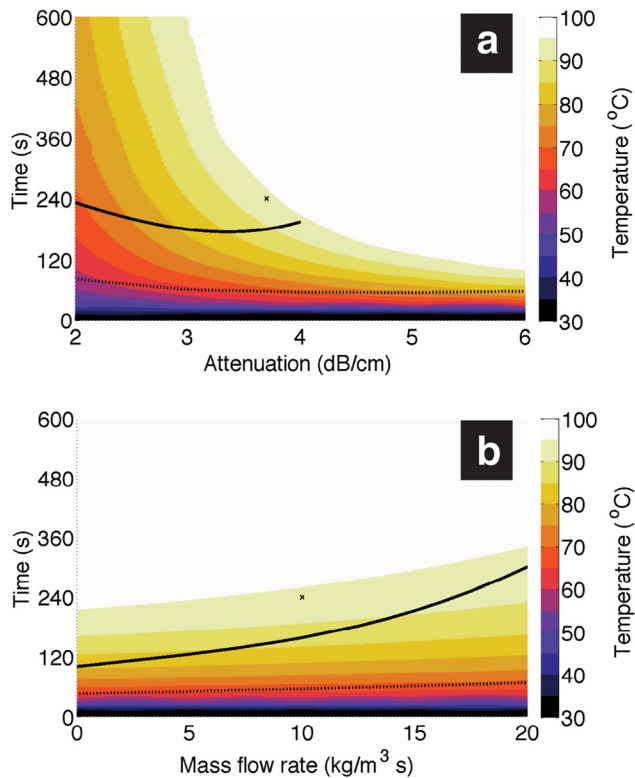


FIG. 8. (Color online) Results of simulations of heating using Eq. (4) assuming a range of values for the (a) attenuation and (b) perfusion in brain. It was assumed that all 56 elements of the applicator were operating at a frequency of 6 MHz and at an output intensity of 30 W/cm^2 . In (a), the mass flow rate was assumed to be constant, $w = 10 \text{ kg/(m}^3 \cdot \text{s)}$, while the attenuation was varied from $\alpha = 2\text{--}6 \text{ dB/cm}$. In (b), the attenuation was assumed to be constant, $\alpha = 3.7 \text{ dB/cm}$, while the mass flow rate was varied from $w = 0\text{--}20 \text{ kg/(m}^3 \cdot \text{s)}$. The maximum temperature reached during heating durations from 0 to 600 s is shown in both plots as well as the time required to create lesions with a depth, R_{max} , of 10 mm (dotted line) and 15 mm (solid line) assuming a thermal dose threshold of $t_{43} = 50 \text{ min}$. The parameters used for the results shown in Fig. 7 are indicated by a cross (x) in each plot.

coefficients, $\alpha = 2\text{--}6 \text{ dB/cm}$, that correspond approximately to the range reported in the literature for the brain.^{33,39} The maximum temperature reached is shown and is plotted for heating durations of up to 600 s. The plots show that as the attenuation coefficient is increased, the maximum temperature reached for a given heating duration increases. At $\alpha = 2 \text{ dB/cm}$, the maximum temperature reached is $75\text{--}80^\circ\text{C}$ after 600 s of heating. As the attenuation is increased to 6 dB/cm , a maximum temperature of greater than 95°C is reached in less than 60 s of heating.

In addition to the maximum temperature, the time required to obtain a lesion with a depth, R_{max} , of 10 mm (dashed line) and 15 mm (solid line) is plotted in Fig. 8(a). These curves demonstrate that although the maximum temperature increases with attenuation, the time required to create a lesion with a given depth is relatively insensitive to the value of attenuation. At an attenuation of 2 dB/cm , the time required to create a lesion with a depth of 10 mm is 90 s while 240 s is required to reach a depth of 15 mm. As the attenuation is increased to 6 dB/cm , the time required is 60 s for $R_{\text{max}} = 10 \text{ mm}$ while a temperature of $>95^\circ\text{C}$ is reached before a depth of 15 mm is reached. This demonstrates that the applicator would have to either be operated at a lower

output power level (i.e., surface intensity of $<30 \text{ W/cm}^2$) to achieve a 15 mm depth lesion or a strategy for pulsing the heating with a duty cycle of $<100\%$ would have to be implemented to avoid reaching boiling temperatures.

In Fig. 8(b), a plot similar to that shown in Fig. 8(a) of maximum temperature and time required for lesion formation is plotted with a varying range of perfusion rates, w , ranging from no perfusion to a value twice that used for the simulation shown in Fig. 7. The output intensity was kept constant at a value of 30 W/cm^2 , and all elements of the transducer were assumed to be active with a fixed attenuation coefficient of $\alpha = 3.7 \text{ dB/cm}$. The results demonstrate that as the perfusion is increased, the maximum temperature reached within a given heating duration quickly decreases. Interestingly, the estimated time required to create a thermal lesion with a depth of 10 mm remains relatively constant across the range of mass flow rates used in simulations while the time required for a lesion with a depth of 15 mm increases from 2 min to more than 5 min, indicating that perfusion has a large effect on the time required to create lesions at depth.

IV. DISCUSSION AND CONCLUSIONS

This study demonstrated the preliminary feasibility of using a 56 element, 4.8-mm diameter interstitial ultrasound applicator for MR-guided thermal ablation in the brain. The device allows for the possibility to perform electronic control through selection of power of each of the elements in both the plane oriented along the probe axis and in the plane perpendicular to the applicator, allowing for the possibility of heating with increased spatial control as compared to existing applicators.

In the first part of this work, the acoustic holography method was used to reconstruct the source vibration to verify that the device was functioning properly. When the source was reconstructed, it was observed that the elements at the center of each of the faces tended to have slightly higher outputs than the elements at the edges, resulting in a higher expected maximum temperature rise when a single face was excited in parallel. Upon further testing of the array, it was found that the electrical impedance of the elements tended to vary regularly along a face and could potentially explain the variation observed in acoustic output. If the variation is attributable to differences in electrical power and not electroacoustic efficiency between the elements, the array output could be normalized by using separate channels for each of the 56 elements of the array (such a system is currently in development). Nevertheless, the results from the acoustic holography method show that this method can be used to better understand the functioning of high frequency arrays, which can be important when operating such devices as the generator system, and electronics components, and device construction can all lead to deviations in the expected output of the individual array elements.

The MR compatibility of the device in the tests performed using a 1.5 T clinical scanner were excellent, in particular near the active face of the array. This aspect of the device is important as the maximum temperature rise occurs

within 4–6 mm of the face of the array (see Figs. 5 and 6). The maximum temperature in the field must be accurately monitored in this area to avoid the possibility of inducing temperatures of over 100°C and tissue boiling during a treatment,⁴⁰ which could potentially pose a risk to the patient and distort significantly the extent of the desired thermal lesion. Although the maximum temperature rise measured here was well below boiling (+29°C, which would be 66°C *in vivo*), the absorption in a tumor,³⁹ reflections from nearby skull bone, or activation of several or all faces at the same time (as shown in Figs. 7 and 8) could result in heating to >100°C. The excellent MR compatibility of the device ensures that heating can be adequately monitored in real time so that thermal ablation can be performed more safely with the device.

The clinical goal of this project is to develop a device that can be used for ablation in brain at depths of more than 15 mm so that tissue masses on the order of 30 mm in diameter can be treated; this is similar to the range of ablation that has been reported in LITT treatments.² To demonstrate that our array has this capability, we first performed *in vitro* measurements to compare numerical simulations with experimental results and then used the model to predict the size of lesions that may be expected *in vivo*.

The results of heating tests in gel phantoms, shown in Fig. 5, demonstrated the basic principle of spatial control that can be achieved with the prototype device. During this experiment, the device was not mechanically rotated and instead heating was performed by selecting various configurations of elements (in this case entire “faces” of eight elements) through software control. In principle, through appropriate selection and control of the duration and intensity of heating in each angular direction, the temperature rise induced and the subsequent lesion depth can be varied.

Given the uncertainty of the exact *in vivo* physical parameters in brain tumors, additional numerical simulations were performed using a range of values for the attenuation and perfusion parameters used in the model to demonstrate that the applicator can be used to treat tumors with diameters of greater than 30 mm. These simulations demonstrated that the applicator is capable of generating a temperature rise of greater than 70°C and lesion depths of >15 mm during heating durations of less than 10 min. Future experiments *in vivo* are planned with the current applicator to verify the results of these simulations.

One limitation of the current design is that with a seven-face multi-faceted planar design, the angular directivity that can be achieved is limited to 360°/7 (51°), thus the thermal lesion resulting from heating in a continuous region around the applicator is expected to have an inhomogeneous border (as shown in Fig. 7). To overcome this limitation when using this type of applicator in clinical use, the existing device could be used with a small manual rotation system (with only two fixed positions for example), and the applicator could be rotated once by the surgeon to complete the treatment if a more homogeneous lesion or finer control was desired at the border.

Alternatively, based on the promising results with the present device, various configurations of the device design

are being explored in numerical simulations that may result in a more homogeneous distribution of the lesion. For example, because the transducer is piezocomposite, it has additional bandwidth that could be exploited for tailoring the lesion shape. The transducer, though operated at 6 MHz, could in theory be operated from 4 to 8 MHz, and thus a different frequency or even a multi-frequency approach⁴¹ could be investigated in more detail for our device and may provide better heating distributions for certain tumor geometries.

ACKNOWLEDGMENTS

This work was supported by CarThera SAS. The authors would like to thank Adrien Matias, Alain Birer, and Alexandre Vignot for help with the design and construction of the experimental setup and Samir Lounis and Remi Souchon for assistance with the MRI measurements. Additionally, we would like to thank the MRI clinic of Lyon-Villeurbanne. M.C. would like to additionally thank the Acoustical Society of America for funding during the initial year (2009–2010) of this project through the F.V. Hunt Postdoctoral Fellowship. The work of S.T. was supported by the Russian Foundation for Basic Research (RFBR 11-02-01189 and 12-02-31925).

¹Y. Anzai, R. Lufkin, A. DeSalles, D. Hamilton, K. Farahani, and K. Black, “Preliminary experience with MR-guided thermal ablation of brain tumors,” *Am. J. Neuroradiol.* **16**, 39–48 (1995).

²A. Carpentier, R. J. McNichols, R. J. Stafford, J. Itzcovitz, J. Guichard, D. Reizine, S. Delalogue, E. Vicaut, D. Payen, A. Gowda, and B. George, “Real-time magnetic resonance-guided laser thermal therapy for focal metastatic brain tumors,” *Neurosurgery* **63**, ons21–ons28 (2008).

³H.-J. Schwarzmaier, F. Eickmeyer, W. von Tempelhoff, V. U. Fiedler, H. Niehoff, S. D. Ulrich, Q. Yang, and F. Ulrich, “MR-guided laser-induced interstitial thermotherapy of recurrent glioblastoma multiforme: Preliminary results in 16 patients,” *Eur. J. Radiol.* **59**, 208–215 (2006).

⁴A. Hawasli, W. Ray, R. Murphy, R. Dacey, Jr., and E. Leuthardt, “Magnetic resonance imaging-guided focused laser interstitial thermal therapy for subinsular metastatic adenocarcinoma: Technical case report,” *Neurosurgery* **70**, onsE332–onsE338 (2012).

⁵G. Rahmathulla, P. Recinos, J. Valerio, S. Chao, and G. Barnett, “Laser interstitial thermal therapy for focal cerebral radiation necrosis: A case report and literature review,” *Stereotact. Funct. Neurosurg.* **90**, 192–200 (2012).

⁶A. Carpentier, D. Chauvet, V. Reina, K. Beccaria, D. Leclercq, R. McNichols, A. Gowda, P. Cornu, and J. Delattre, “MR-Guided LITT for recurrent glioblastomas,” *Lasers. Surg. Med.* **44**, 361–368 (2012).

⁷Z. Ram, Z. R. Cohen, S. Harnof, S. Tal, M. Faibel, D. Nass, S. Maier, M. Hadani, and Y. Mardor, “Magnetic resonance imaging-guided, high-intensity focused ultrasound for brain tumor therapy,” *Neurosurgery* **59**, 949–955 (2006).

⁸P. Jethwa, J. Barrese, A. Gowda, A. Shetty, and S. Danish, “Magnetic resonance thermometry guided laser induced thermal therapy (LITT) for intracranial neoplasms: Initial experience,” *Neurosurgery* **71**, ons133–ons145 (2012).

⁹N. McDannold, “Quantitative MRI-based temperature mapping based on the proton resonant frequency shift: Review of validation studies,” *Int. J. Hyperthermia* **21**, 533–546 (2005).

¹⁰M. Pernot, J. F. Aubry, M. Tanter, A. Boch, F. Marquet, M. Kujas, D. Seilhean, and M. Fink, “In vivo transcranial brain surgery with an ultrasonic time reversal mirror,” *J. Neurosurg.* **106**, 1061–1066 (2007).

¹¹N. McDannold, G. Clement, P. Black, F. Jolesz, and K. Hynynen, “Transcranial magnetic resonance imaging-guided focused ultrasound surgery of brain tumors: Initial findings in 3 patients,” *Neurosurgery* **66**, 323–332 (2010).

¹²C. Herickhoff, E. Light, K. Bing, S. Mukundan, G. Grant, P. Wolf, and S. Smith, “Dual-mode intracranial catheter integrating 3D ultrasound

- imaging and hyperthermia for neuro-oncology: Feasibility study," *Ultrason. Imaging* **31**, 81–100 (2009).
- ¹³C. Lafon, D. Melodelima, R. Salomir, and J. Y. Chapelon, "Interstitial devices for minimally invasive thermal ablation by high-intensity ultrasound," *Int. J. Hyperthermia* **23**, 153–163 (2007).
- ¹⁴K. Gentry and S. Smith, "Integrated catheter for 3-D intracardiac echo cardiography and ultrasound ablation," *IEEE Trans. Ultrason. Ferroelectr. Freq. Control* **51**, 800–808 (2004).
- ¹⁵D. Melodelima, C. Lafon, F. Prat, Y. Theillere, A. Arefiev, and D. Cathignol, "Transoesophageal ultrasound applicator for sector-based thermal ablation: First in vivo experiments," *Ultrasound Med. Biol.* **29**, 285–291 (2003).
- ¹⁶T. Mast, P. Barthe, I. Makin, M. Slayton, C. Karunakaran, S. Burgess, A. Alqadah, and S. Rudich, "Treatment of rabbit liver cancer in vivo using miniaturized image-ablate ultrasound arrays," *Ultrasound Med. Biol.* **37**, 1609–1621 (2011).
- ¹⁷T. Mast, I. Makin, W. Faidi, M. Runk, P. Barthe, and M. Slayton, "Bulk ablation of soft tissue with intense ultrasound: Modeling and experiments," *J. Acoust. Soc. Am.* **118**, 2715–2724 (2005).
- ¹⁸M. Kangasniemi, C. Diederich, R. Price, R. Stafford, D. Schomer, L. Olsson, P. Tyreus, W. Nau, and J. Hazle, "Multiplanar MR temperature-sensitive imaging of cerebral thermal treatment using interstitial ultrasound applicators in a canine model," *J. Magn. Reson. Imaging* **16**, 522–531 (2002).
- ¹⁹C. Lafon, J. Y. Chapelon, F. Prat, F. Gorry, J. Margonari, Y. Theilliere, and D. Cathignol, "Design and preliminary results of an ultrasound applicator for interstitial thermal coagulation," *Ultrasound Med. Biol.* **24**, 113–122 (1998).
- ²⁰E. Delabrousse, R. Salomir, A. Birer, C. Paquet, F. Mittieux, J. Y. Chapelon, F. Cotton, and C. Lafon, "Automatic temperature control for MR-guided interstitial ultrasound ablation in liver using a percutaneous applicator: Ex vivo and in vivo initial studies," *Magn. Reson. Med.* **63**, 667–679 (2010).
- ²¹R. Chopra, M. J. Bronskill, and F. S. Foster, "Feasibility of linear arrays for interstitial ultrasound thermal therapy," *Med. Phys.* **27**, 1281–1286 (2000).
- ²²R. Chopra, N. Baker, V. Choy, A. Boyes, K. Tang, D. Bradwell, and M. J. Bronskill, "MRI-compatible transurethral ultrasound system for the treatment of localized prostate cancer using rotational control," *Med. Phys.* **35**, 1346–1357 (2008).
- ²³K. Siddiqui, R. Chopra, S. Vedula, L. Sugar, M. Haider, A. Boyes, M. Musquera, M. Bronskill, and L. Klotz, "MRI-guided transurethral ultrasound therapy of the prostate gland using real-time thermal mapping: Initial studies," *Urology* **76**, 1506–1511 (2010).
- ²⁴N. Owen, G. Bouchoux, B. Seket, A. Murillo-Rincon, S. Merouche, A. Birer, C. Paquet, E. Delabrousse, J. Chapelon, R. Berriet, G. Fleury, and C. Lafon, "In vivo evaluation of a mechanically oscillating dual-mode applicator for ultrasound imaging and thermal ablation," *IEEE Trans. Biomed. Eng.* **57**, 80–92 (2010).
- ²⁵C. Diederich, W. Nau, E. Burdette, I. Bustany, D. Deardorff, and P. Stauffer, "Combination of transurethral and interstitial ultrasound applicators for high-temperature prostate thermal therapy," *Int. J. Hyperthermia* **16**, 385–403 (2000).
- ²⁶D. Melodelima, R. Salomir, C. Mougenot, C. Moonen, and D. Cathignol, "64-element intraluminal ultrasound cylindrical phased array for transesophageal thermal ablation under fast MR temperature mapping: An ex vivo study," *Med. Phys.* **33**, 2926–2934 (2006).
- ²⁷O. Sapozhnikov, Y. Pishchal'nikov, and A. Morozov, "Reconstruction of the normal velocity distribution on the surface of an ultrasonic transducer from the acoustic pressure measured on a reference surface," *Acoust. Phys.* **49**, 416–424 (2003).
- ²⁸G. Clement and K. Hynynen, "Field characterization of therapeutic ultrasound phase arrays through forward and backward planar projection," *J. Acoust. Soc. Am.* **108**, 441–446 (2000).
- ²⁹S. Tsygar, O. Sapozhnikov, C. Lafon, T. Charrel, and M. Canney, "Improving acoustic holography of ultrasonic transducers based on their virtual shifts and rotation relative to a field-mapping surface," in *Book of Abstracts of the International Congress on Ultrasonics ICU 2011*, edited by B. Linde, A. Markiewicz, and N. Ponikwicki (University of Gdansk Publishing, Gdansk, Poland, 2011), pp. 337–338.
- ³⁰B. Quesson, J. de Zwart, and C. Moonen, "Magnetic resonance temperature imaging for guidance of thermotherapy," *J. Magn. Reson. Imaging* **12**, 525–533 (2000).
- ³¹A. Chung, K. Hynynen, V. Colucci, K. Oshio, H. Cline, and F. Jolesz, "Optimization of spoiled gradient-echo phase imaging for in vivo localization of a focused ultrasound beam," *Magn. Reson. Med.* **36**, 745–752 (1996).
- ³²C. Lafon, V. Zderic, M. Noble, J. Yuen, P. Kaczkowski, O. Sapozhnikov, F. Chavrier, L. Crum, and S. Vaezy, "Gel phantom for use in high-intensity focused ultrasound dosimetry," *Ultrasound Med. Biol.* **31**, 1383–1389 (2005).
- ³³F. Kremkau, R. Barnes, and C. McGraw, "Ultrasonic attenuation and propagation speed in normal human brain," *J. Acoust. Soc. Am.* **70**, 29–38 (1981).
- ³⁴F. Duck, *Physical Properties of Tissue: A Comprehensive Reference Book* (Academic, San Diego, 1990), pp. 9–124.
- ³⁵J. Yung, A. Shetty, A. Elliott, J. Weinberg, R. McNichols, A. Gowda, J. Hazle, and R. Stafford, "Quantitative comparison of thermal dose models in normal canine brain," *Med. Phys.* **37**, 5313–5321 (2010).
- ³⁶L. Chen, J. P. Wansapura, G. Heit, and K. Butts, "Study of laser ablation in the in vivo rabbit brain with MR thermometry," *J. Magn. Reson. Imaging* **16**, 147–152 (2002).
- ³⁷N. McDannold, N. Vykhodtseva, F. Jolesz, and K. Hynynen, "MRI investigation of the threshold for thermally induced blood-brain barrier disruption and brain tissue damage in the rabbit brain," *Magn. Reson. Med.* **51**, 913–923 (2004).
- ³⁸R. Stafford, R. Price, C. Diederich, M. Kangasniemi, L. Olsson, and J. Hazle, "Interleaved echo-planar imaging for fast multiplanar magnetic resonance temperature imaging of ultrasound thermal ablation therapy," *J. Magn. Reson. Imaging* **20**, 706–714 (2004).
- ³⁹S. Goss, R. Johnston, and F. Dunn, "Comprehensive compilation of empirical ultrasonic properties of mammalian tissues," *J. Acoust. Soc. Am.* **64**, 423–457 (1978).
- ⁴⁰T. Khokhlova, M. Canney, D. Lee, K. Marro, L. Crum, V. Khokhlova, and M. Bailey, "Magnetic resonance imaging of boiling induced by high intensity focused ultrasound," *J. Acoust. Soc. Am.* **125**, 2420–2431 (2009).
- ⁴¹R. Chopra, C. Luginbuhl, F. Foster, and M. Bronskill, "Multifrequency ultrasound transducers for conformal interstitial thermal therapy," *IEEE Trans. Ultrason. Ferroelectr. Freq. Control* **50**, 881–889 (2003).